Normalised hybrid flux weakening strategy for automotive asymmetrical dual three-phase IPMSMs

A. Navarro-Temoche[1], E. Ibarra[1], I. Kortabarria[1], A. Sierra-González[2], B. Prieto[3], I. Elosegui[3]
[1]University of the Basque Country (UPV/EHU)
[2]TECNALIA, Basque Research and Technology Alliance (BRTA)
[3]Transport & Energy Division, Ceit BRTA & University of Navarra School of Engineering
adrianorai.navarro@ehu.eus

***Abstract*—In this paper, a hybrid flux weakening control strategy based on a vector space decomposition (VSD) model is presented for asymmetrical dual three-phase interior permanent magnet synchronous machines (IPMSMs). This strategy integrates a voltage magnitude feedback loop, which provides robustness against deviations in the electrical parameters of the machine, by acting on the angle of the current vector; and a feed-forward to improve the controller action. In parallel, the current vector is analytically determined in a normalised system. Simulation results that evaluate the performance of the controller over standardised driving cycles demonstrate the validity of the proposal.**

***Index Terms*—Dual three-phase, IPMSM, EV, flux weakening**

I. Introduction

Interior Permanent magnet synchronous machines (IPMSMs) are widely used in both Electric Vehicle (EV) and Hybrid EV (HEV) applications. These machines are compact and exhibit high power density and high efficiency [1]. In addition, the reduced per-phase power, torque ripple, low harmonic content and improved fault tolerance of multi-phase technologies over conventional three-phase systems make them attractive for applications with high power and reliability requirements [2].

Dual three-phase configuration is one of the most studied multi-phase architecture. Depending on the phase arrangement between the three-phase sets, they can be classified as symmetrical (shifted by 0 or $\pi/3$) or asymmetrical (shifted by $\pi/6$). With the latter configuration (Fig. 1), sixth harmonic torque pulsations produced by the two winding sets are in anti-phase and, therefore, they are cancelled [3].

Regardless of such phase shift, vector control strategies for dual three-phase IPMSMs can be broadly divided into two categories: the ones using two individual current controllers, based on the double dq synchronous frames model with mutual coupling voltages between both frames [4], [5]; and the ones based on vector space decomposition (VSD) control, with two currents regulators per each generated sub-plane [6], [7]. The latter techniques are prevailing since there is not mutual coupling between sub-planes and, as a result, a more accurate torque regulation can be provided [8].

To extend the operating speed range of an EV drive, which is constrained by the battery voltage, flux weakening (FW) needs to be applied. FW strategies can be classified into the *feed-forward*, where Look-up Tables (LUTs) or analytical calculations are used [9]–[11], *feedback* [12], [13], and *hybrid* [14] families. For example, the Vector Current Control (VCC) approach is the most commonly adopted feedback-based FW alternative, where three types of regulation are possible: on voltage magnitude [15]–[17], voltage error [10], and duty cycles [18].

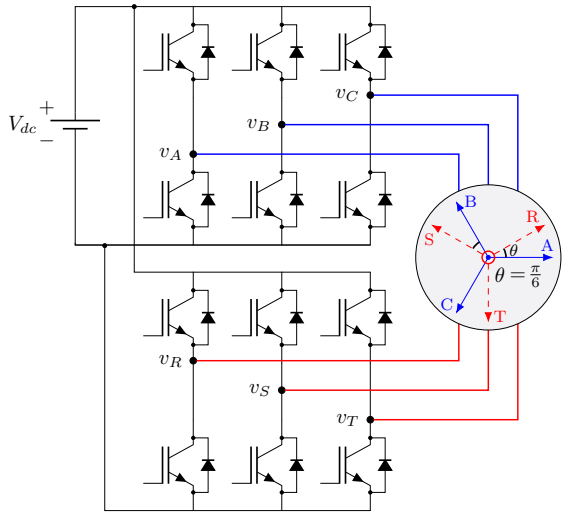

Fig. 1. Dual three-phase PMSM drive system.

A hybrid flux weakening control strategy is proposed, which uses a VCC to regulate the voltage magnitude considering the current angle variation as output, as suggested by Bolognani in [15]. In addition, to improve the performance of the FW algorithm, a *feed-forward* technique is integrated, where current trajectories are analytically determined in a normalised system depending on the angle position of the current vector. [17], [19].

This paper is organised as follows: In section II, the mathematical model of a dual-three phase IPMSMs is briefly introduced. Achievable operating regions are introduced in Section III. The hybrid flux weakening control based on a normalised system is developed in Section IV. Finally, simulation results are presented and discussed in Section IV and conclusions are provided.

II. Mathematical model of an asymmetrical dual three-phase PMSM

According to the VSD theory [6], the six-dimensional machine, represented in the *ABC-XYZ* frame, can be decomposed into three orthogonal sub-spaces: $\alpha\beta, z_1z_2$ and o_1o_2. By applying the transformation matrix T_6 of (2), harmonics in the *ABC-XYZ* frame are mapped into different sub-planes: The fundamental and $(12k \pm 1)$th, $k = 1, 2, \ldots$ harmonics are mapped into $\alpha\beta$; the $(6k \pm 1)$th, $k = 1, 3, 5, \ldots$ into z_1z_2; and the $(3k)$th, $k = 0, 1, 3, 5, \ldots$ into o_1o_2 sub-plane. Thus,

$$\begin{bmatrix} F_\alpha & F_\beta & F_{z_1} & F_{z_2} & F_{o_1} & F_{o_2} \end{bmatrix}^T = [T_6] \begin{bmatrix} F_A & F_B & F_C & F_X & F_Y & F_Z \end{bmatrix}^T, \quad (1)$$

$$[T_6] = \frac{1}{3} \begin{bmatrix} 1 & \cos(4\theta_s) & \cos(8\theta_s) & \cos(\theta_s) & \cos(5\theta_s) & \cos(9\theta_s) \\ 0 & \sin(4\theta_s) & \sin(8\theta_s) & \sin(\theta_s) & \sin(5\theta_s) & \sin(9\theta_s) \\ 1 & \cos(8\theta_s) & \cos(4\theta_s) & \cos(5\theta_s) & \cos(\theta_s) & \cos(9\theta_s) \\ 0 & \sin(8\theta_s) & \sin(4\theta_s) & \sin(5\theta_s) & \sin(\theta_s) & \sin(9\theta_s) \\ 1 & 1 & 1 & 0 & 0 & 0 \\ 0 & 0 & 0 & 1 & 1 & 1 \end{bmatrix}, \quad (2)$$

where $\theta_s = \pi/6$.

The variables in the $\alpha\beta$ sub-plane can be converted into the dq synchronous frame by applying the standard Park transformation, and the variables in z_1z_2 can be converted to a new frame, designated as d_zq_z [20]:

$$\begin{bmatrix} F_d \\ F_q \end{bmatrix} = \begin{bmatrix} \cos\theta_e & \sin\theta_e \\ -\sin\theta_e & \cos\theta_e \end{bmatrix} \begin{bmatrix} F_\alpha \\ F_\beta \end{bmatrix} = \mathbf{T_{dq}} F_{\alpha\beta}, \quad (3)$$

where F can be voltage (v), current (i) or flux (ψ). Then, the $(6k \pm 1)$th, $k = 1, 3, 5, \ldots$ harmonics in z_1z_2 sub-plane are converted to $(6k)$th harmonics in the d_zq_z-frame:

$$\begin{bmatrix} F_{dz} \\ F_{qz} \end{bmatrix} = \begin{bmatrix} -\cos\theta_e & \sin\theta_e \\ \sin\theta_e & \cos\theta_e \end{bmatrix} \begin{bmatrix} F_{z_1} \\ F_{z_2} \end{bmatrix} = \mathbf{T_{d_zq_z}} F_{z_1z_2}. \quad (4)$$

The mathematical model of a dual three-phase IPMSM by means of VSD is detailed in [8], where the voltage equations in the dq-frame ($\alpha\beta$ sub-plane) and d_zq_z-frame (z_1z_2 sub-plane) can be expressed as:

$$\begin{bmatrix} v_d \\ v_q \end{bmatrix} = \begin{bmatrix} R_s + L_d^{eq}s & 0 \\ 0 & R_s + L_q^{eq}s \end{bmatrix} \begin{bmatrix} i_d \\ i_q \end{bmatrix} + \omega_e \begin{bmatrix} -L_q^{eq} i_q \\ L_d^{eq} i_d + \lambda_m \end{bmatrix}, \quad (5)$$

$$\begin{bmatrix} v_{dz} \\ v_{qz} \end{bmatrix} = \begin{bmatrix} R_s + L_{dz}s & 0 \\ 0 & R_s + L_{qz}s \end{bmatrix} \begin{bmatrix} i_{dz} \\ i_{qz} \end{bmatrix} + \omega_e \begin{bmatrix} -L_{qz} i_{qz} \\ L_{dz} i_{dz} \end{bmatrix}, \quad (6)$$

where λ_m is the PM flux linkage and ω_e is the electrical speed. If full mutual coupling between the two sets and full mutual coupling between phases in each set are assumed, the equivalent inductances L_d^{eq} and L_q^{eq} in the dq-frame, and L_{dz} and L_{qz} in the dqz-frame can be simplified as:

$$L_d^{eq} = L_{sl} + 3L_d \ , \ L_q^{eq} = L_{sl} + 3L_q, \quad (7)$$

$$L_{dz} = L_{sl} \ , \ L_{qz} = L_{sl}. \quad (8)$$

As can be seen from (5) and (6), the i_d and i_q currents projected in the dq-frame are related to energy conversion whereas the ones in the d_zq_z-frame (i_{dz}, i_{qz}) make no contribution to torque generation [6]. Thus, the electromagnetic torque is expressed as:

$$T_{em} = 3N_p[\lambda_m + (L_d^{eq} - L_q^{eq})i_d]i_q, \quad (9)$$

where N_p is the pole-pair number.

TABLE I
Base values for IPMSMs [19].

Parameter	Value	Parameter	Value
Base electrical speed ω_b	$\omega_{e,N}$	Base current I_b	λ_m/L_d^{eq}
Base voltage V_b	$\lambda_m\omega_{e,N}$	Base torque T_b	$3N_p\lambda_m^2/L_d^{eq}$
Saliency ξ	L_q^{eq}/L_d^{eq}		

III. Operation regions of the dual three-phase IPMSM drive

In this section, the dual three-phase IPMSM is described in a normalised system to simplify the analysis of the operation regions of the drive. Table I collects the base values. Regarding the achievable operation points, they are restricted by the current and voltage limits of the drive. The normalised maximum current ($\bar{i}_{max}$) is [21]:

$$\sqrt{\bar{i}_d^2 + \bar{i}_q^2} = \bar{i}_s \leq \bar{i}_{max} = \frac{min(I_{mach,max}, I_{inv,max})}{I_b}, \quad (10)$$

where $\bar{i}_d$ and $\bar{i}_q$ are dq-frame current components, expressed in the normalised system, $\bar{i}_s$ is the normalised modulus of the current vector, $I_{mach,max}$ is the maximum machine current, $I_{inv,max}$ is the maximum inverter current, and I_b is the base current, which value is shown in Table I. Thus, $\bar{i}_{max}$ can be higher or lower than 1, depending whether the machine and inverter current limits are higher or lower than I_b.

The normalised maximum voltage produced by the inverter without over-modulation ($\bar{v}_{max}$) [22] is expressed as:

$$\sqrt{\bar{v}_d^2 + \bar{v}_q^2} = \bar{v}_s \leq \bar{v}_{max} = \frac{V_{dc}}{\sqrt{3}V_b}, \quad (11)$$

where $\bar{v}_d$ and $\bar{v}_q$ are the dq frame voltage components expressed in the normalised system, $\bar{v}_s$ is the normalised modulus of the voltage vector, V_{dc} is the DC voltage bus, and V_b is the base value of the voltage indicated in Table I. It is worth noting that the limit in (11) depends on the used modulation strategy ($V_{dc}/\sqrt{3}$ for space vector modulation or PWM with third harmonic injection).

By normalising (5), considering steady state operation and neglecting the voltage drop related to the stator resistance R_s, the voltage limit can be rewritten as [22]:

$$\begin{matrix} \bar{v}_d = -\bar{i}_q\Omega_e\xi, \\ \bar{v}_q = \Omega_e(\bar{i}_d + 1), \end{matrix} \rightarrow \frac{(\bar{i}_d + 1)^2}{(\frac{\bar{v}_{max}}{\Omega_e})^2} + \frac{\bar{i}_q^2}{(\frac{\bar{v}_{max}}{\Omega_e\xi})^2} \leq 1, \quad (12)$$

where Ω_e is the normalised electrical speed. The voltage limit in (12) can be described as an ellipse with the center in $(\bar{i}_d, \bar{i}_q) = (-1, 0)$, in which semi-major and semi-minor axes are equal to $\bar{v}_s/\Omega_e$ and $\bar{v}_s/\Omega_e\xi$, respectively. If the voltage curve centre is located inside the current circle ($\bar{i}_{max} > 1$), the

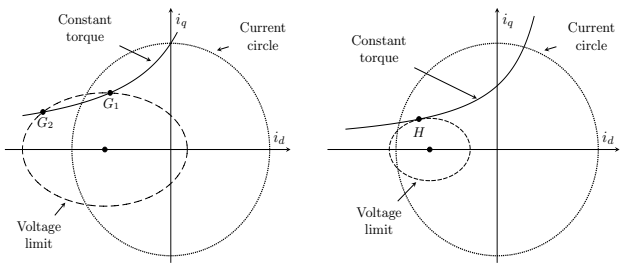

(a) FW (b) MTPV

Fig. 2. Flux weakening scenarios [23].

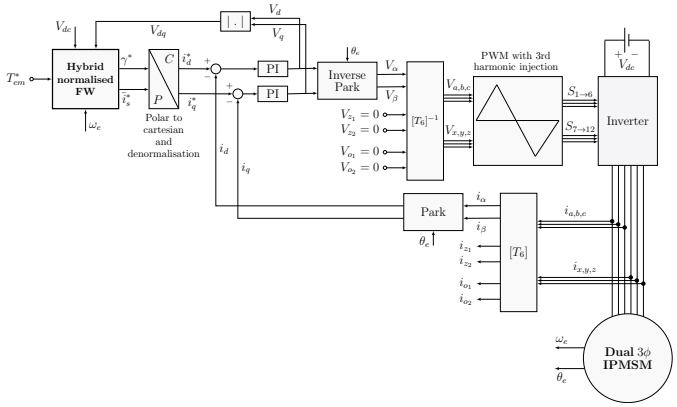

Fig. 3. Field oriented control (FOC) of dual three-phase machine incorporating proposed set-point generation algorithm.

theoretical maximum achievable speed is not finite. Otherwise, the maximum speed is finite at point $(\bar{i}_d, \bar{i}_q) = (-1, 0)$, see Fig. 2.

On the other hand, by normalising (9), the electromagnetic torque (τ_{em}) is expressed as:

$$\tau_{em} = \bar{i}_q[1 + (1 - \xi)\bar{i}_d], \tag{13}$$

were several $\bar{i}_d$ and $\bar{i}_q$ combinations that lead to the same torque value can be obtained. Thus, proper current trajectory calculations are fundamental if losses are required to be reduced. In accordance with (10) and (11), four regions can be distinguished for a synchronous machine: Maximum Torque per Ampere (MTPA) region, Flux Weakening (FW) region (without and with torque reduction) and Maximum Torque per Voltage (MTPV) region, also known as deep flux weakening region.

A maximum torque per applied current modulus is guaranteed in the MTPA trajectory, and ohmic losses are minimised, which prevail at low speeds [23]. A MTPA point is applicable provided that it is not located beyond the ellipse related to the voltage limit. Otherwise, flux weakening mode is reached and a new current angle and current magnitude must be calculated to guarantee minimum phase currents. The FW trajectory (Fig. 2(a)) is referred to the vectors intersecting the reference torque curve (G_1 and G_2 points). The reference torque is maintained through this trajectory until reaching the current limit, where it decreases. Finally, the MTPV trajectory is defined as the curve where the maximum torque is reached with a minimum voltage (H point which intersects a maximum torque curve for a voltage limit is shown in Fig. 2(b)). This trajectory minimises magnetic losses, which are prevalent at high speeds.

IV. Flux weakening control based on a normalised system

A. General description

In this paper, a hybrid flux weakening control strategy that considers all the aforementioned operation regions and determines the current reference trajectories from equations expressed in a normalised system is proposed. This algorithm is integrated in the Field Oriented Control (FOC) as shown in Fig. 3. Note that only the dq sub-plane is used by the controller.

Considering $\bar{i}_d$ and $\bar{i}_q$ in terms of angle and magnitude, an angular displacement ($\Delta\gamma^f$) is added to the MTPA angle (γ_M) to obtain a reference current angle (γ^*), which is used to maintain the stator voltage modulus inside the voltage limit (Fig. 4(a)). Thus, the operating range of γ^* is bounded by $[\gamma_M; \pi]$.

The term $\Delta\gamma^f$ (Fig. 4(a)) is determined from a feed-forward block, which calculates the theoretical displacement of the current angle ($\Delta\gamma^a$) from the torque reference (τ^*_{em}) and the normalised electrical speed (ω_e); and a voltage feedback controller, providing $\Delta\gamma^r$. The latter aims to compensate errors in the determination of the analytic FW trajectory due to possible parameter deviations in the drive system.

Regarding the current reference magnitude determination, magnitudes that correspond to the MTPV trajectory (i_{mtpv}) and to the magnitude required to achieve the set-point torque (i_{tem}) are determined (Fig. 4(b)). Depending on the position of γ^*, two dynamic saturation blocks provide a smooth transition between all the operating regions. To obtain the final reference current magnitude $\bar{i}^*_s$, without exceeding the $\bar{i}_{max}$ limit, i_{tem} is saturated by i_{mtpv} as upper limit, provided that the latter does not exceed the current limit $\bar{i}_{max}$. Otherwise, the upper limit is equal to $\bar{i}_{max}$.

B. MTPA angle calculation

For synchronous machines, the MTPA currents ($\bar{i}_{d_M}$ and $\bar{i}_{q_M}$) are obtained for a given torque reference [23]:

$$\tau^*_{em} = \frac{\bar{i}_{q_M}}{2}[1 + \sqrt{1 + 4(1 - \xi)^2\bar{i}^2_{q_M}}], \tag{14}$$

$$\tau^*_{em} = \sqrt{\frac{\bar{i}_{d_M}}{1 - \xi}[1 + (1 - \xi)\bar{i}_{d_M}]^3}. \tag{15}$$

In this way, the MTPA angle (γ_M) is obtained as:

$$\gamma_M = \arccos\frac{\bar{i}_{d_M}}{\bar{i}_{s_M}} \longrightarrow \bar{i}^2_{s_M} = \bar{i}^2_{d_M} + \bar{i}^2_{q_M}. \tag{16}$$

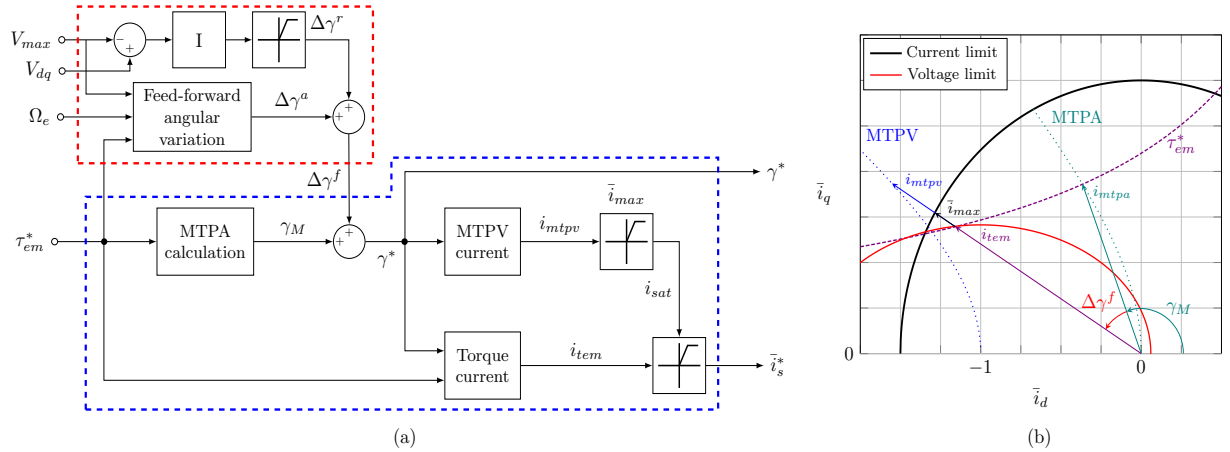

Fig. 4. Proposed hybrid flux weakening control strategy.

C. Feed-forward angular displacement calculation

With respect to the the optimal currents in FW, these can be determined by considering the following optimisation problem [23]:

$$\begin{aligned} \min \quad & \left(L_d^{eq}\left[i_d+\frac{\lambda_m}{L_d^{eq}}\right]\right)^2+\left(L_q^{eq}i_q\right)^2\leq\left(V_{max}/\omega_e\right)^2, \\ s.t \quad & T_{em}=3N_p[\lambda_m+(L_d^{eq}-L_q^{eq})i_d]i_q, \end{aligned} \tag{17}$$

and a fourth order polynomial is obtained in terms of i_d [23]. This polynomial can be normalised with the base values indicated in Table I:

$$\bar{i}_d^4+A_n\bar{i}_d^3+B_n\bar{i}_d^2+C_n\bar{i}_d+D_n=0, \tag{18}$$

where,

$$A_n=\tfrac{2(2-\xi)}{1-\xi}\ ,\ B_n=\tfrac{1}{(1-\xi)^2}+\tfrac{4}{1-\xi}+1-\bar{v}_{max}^2/\Omega_e^2, \tag{19}$$

$$C_n=2\left[\frac{1}{(1-\xi)^2}+\frac{1}{1-\xi}(1-\bar{v}_{max}^2/\Omega_e^2)\right], \tag{20}$$

$$D_n=\frac{1}{(1-\xi)^2}\left[1+\tau_{em}^2\xi^2-\bar{v}_{max}^2/\Omega_e^2\right]. \tag{21}$$

Analytical solution of (18) can be obtained by means of Ferrari's method, thoroughly detailed in [23]:

$$(\bar{i}_d^{FW},\bar{i}_q^{FW})=\left(-\frac{A_n}{4}-\frac{\eta}{2}+\frac{\mu}{2},\frac{\tau_{em}}{1+(1-\xi)\bar{i}_d^{FW}}\right). \tag{22}$$

On the other hand, normalising the MTPV trajectories defined in [23], the following is obtained:

$$\bar{i}_d^{MTPV}=\frac{-\xi+\sqrt{\xi^2+8(\bar{v}_s/\Omega_e)^2(1-\xi)^2}}{4(1-\xi)}-1, \tag{23}$$

$$\bar{i}_q^{MTPV}=\frac{1}{\xi}\sqrt{(\bar{v}_s/\Omega_e)^2-(\bar{i}_d^{MTPV}+1)^2}. \tag{24}$$

Once both FW and MTPV currents have been obtained, it is necessary to define the angle variation in all operating regions:

$$\Delta\gamma_{MTPA}=0\ ,\ \Delta\gamma_{FW}=\arctan(\bar{i}_q^{FW}/\bar{i}_d^{FW})+\pi-\gamma_M, \tag{25}$$

$$\Delta\gamma_{MTPV}=\arctan(\bar{i}_q^{MTPV}/\bar{i}_d^{MTPV})+\pi-\gamma_M. \tag{26}$$

Therefore, $\Delta\gamma^a$ is determined depending on the following conditions:

$$\Delta\gamma^a=\begin{cases}\Delta\gamma_{MTPA} & \text{if} \quad \Delta\gamma_{FW}\leq 0 \mid \bar{i}_d^{MTPV}\leq\bar{i}_d^{FW},\\ \Delta\gamma_{FW} & \text{if} \quad \Delta\gamma_{FW}>0 \mid \bar{i}_d^{MTPV}\leq\bar{i}_d^{FW},\\ \Delta\gamma_{MTPV} & \textit{otherwise.}\end{cases} \tag{27}$$

It is worth highlighting that $\Delta\gamma^a$ is calculated without taking into account the voltage drop produced by R_s. Thus, a feedback voltage loop is included to compensate stator voltage excesses caused by neglecting the influence of R_s or produced due to electrical parameter deviations.

Finally, γ^* is defined as the sum of the analytically calculated angular displacement ($\Delta\gamma^a$), the MTPA angle (γ_M) and the output of the integral controller ($\Delta\gamma^r$).

D. Current magnitude calculation

Finally, both i_{mtpv} and i_{tem} magnitudes are calculated. For i_{tem} determination, the total angular displacement $\Delta\gamma^f$ needs to be considered. If $\Delta\gamma^f=0$, i_{tem} must have the value corresponding to the MTPA trajectory for γ^*, which is obtained by solving $\partial\tau_{em}/\partial\gamma=0$; otherwise, i_{tem} is related to the FW region, and the voltage limit has to be taken into account. Thus, i_{tem} is obtained by applying Ferrari's method to (18), providing i_d in terms of angle and magnitude.

On the other hand, the MTPV condition for synchronous machines is expressed as $\partial\tau_{em}/\partial\delta=0$. Considering the currents in (13) with respect to $\bar{i}_s$ and δ, where the latter is the angle of the voltage vector referred to positive d axis [19], voltages in normalised dq-frame are rewritten as:

$$\begin{aligned}\bar{v}_d&=\bar{v}_s\cos\delta=-\bar{i}_q\Omega_e\xi=-\Omega_e\xi\bar{i}_s\sin\gamma,\\ \bar{v}_q&=\bar{v}_s\sin\delta=\Omega_e(\bar{i}_d+1)=\Omega_e(\bar{i}_s\cos\gamma+1).\end{aligned} \tag{28}$$

and, in consequence,

$$\tfrac{\partial\tau_{em}}{\partial\delta}=\tfrac{(1-\xi)}{\Omega_e^2\xi}[\bar{v}_s^2\cos^2\delta-\bar{v}_s^2\sin^2\delta]-\tfrac{\bar{v}_s\sin\delta}{\Omega_e}=0. \tag{29}$$

By replacing voltage vector terms with expressions in terms of $\bar{i}_s$ and γ, (29) can be rewritten as:

$$\frac{(1-\xi)}{\xi}[(\bar{i}_s\sin\gamma)^2\xi^2-(\bar{i}_s\cos\gamma+1)^2]=\bar{i}_s\cos\gamma+1. \tag{30}$$

TABLE II
PARAMETERS OF THE DUAL THREE-PHASE IPMSM DRIVE.

Parameter	Value	Parameter	Value
Number of pole pairs N_p	19	Stator resistance R_s	61.43 [$m\Omega$]
Equivalent d-axis inductance L_d^{eq}	1.00 [mH]	Equivalent q-axis inductance L_q^{eq}	1.35 [mH]
PM flux linkage λ_m	0.038 [Wb]	DC bus nominal voltage V_{dc}	400 [V]
Maximum torque T_{max}	54 [N.m]	Maximum mech. speed ω_m	5000 [rpm]
Switching frequency	25 [kHz]	Simulation step	1 [μs]

Therefore, (30) is solved as a function of γ, and the MTPV current modulus is defined, in terms of cosines, as:

$$\mathbf{i_{mtpv}} = \frac{-(2-\xi)\cos(\gamma) - \sqrt{(2-\xi)^2\cos(\gamma)^2 - 4(1-\xi)(\cos(\gamma)^2(\xi^2+1)-\xi^2)}}{2(1-\xi)(\cos(\gamma)^2(\xi^2+1)-\xi^2)}. \tag{31}$$

V. SIMULATION RESULTS

A detailed model of an asymmetrical dual three-phase IPMSM drive, whose most relevant parameters are listed in Table II, has been implemented in the Matlab/Simulink environment together with the proposed controller. The field weakening algorithm has been tested under close-to-real driving conditions. In particular, the torque and speed profiles have been calculated for a given EV which is circulating under the New European Driving Cycle (NEDC). Considering the high computational burden of the model, the model has been loaded into an OPAL-RT OP4510 real-time digital platform (Intel Xeon E3 v5 CPU, 4 core, 8 MB cache, 3.5 GHz) and executed in the simulation mode (no real-time). This way, the simulation of the complete NEDC cycle has been carried out in less than 1 hour of execution time. As the field weakening algorithm only enters when the vehicle operates at high speeds, the presented simulations only focus on the extra urban driving profile interval of the NEDC.

Fig. 5(a) shows how, depending on the operation conditions of the drive system, the current set-point generation block calculates online the current reference angle $\gamma^* = \gamma_M + \Delta\gamma^f$ and magnitude i_s^*. Note how, in this particular drive system, the MTPV trajectory is outside the maximum current circle and, thus, this mode of operation does not enter. Once transformed into the dq frame, the d- and q-axis reference currents are determined and regulated by means of the FOC algorithm (Fig. 5(b)). This way, the stator voltage V_{dq} is kept below the maximum limit V_{lim} during the whole driving profile (Fig. 5(c)).

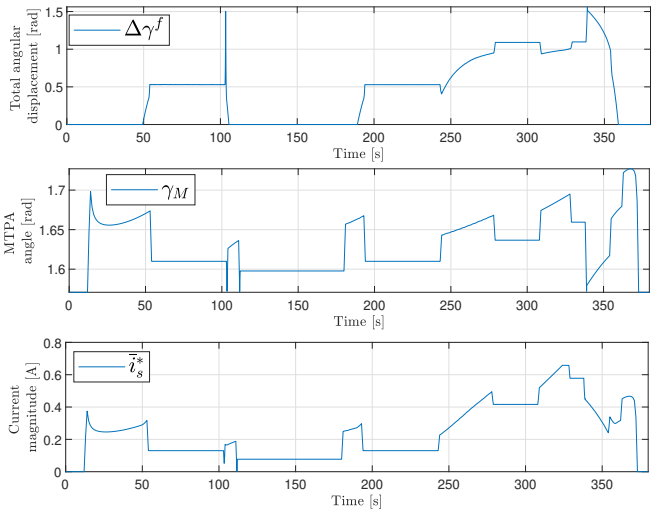

(a) Angle and magnitude determination provided by the proposed set-point generation algorithm.

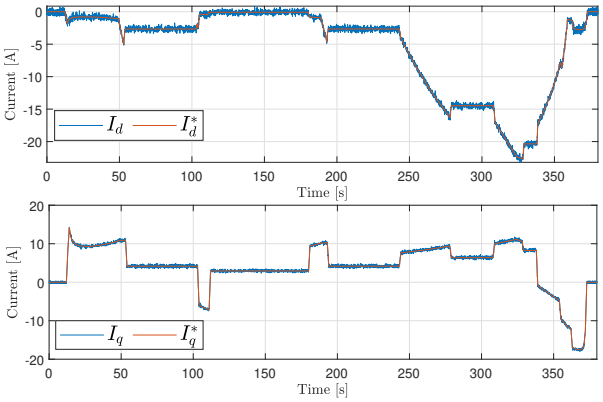

(b) dq currents.

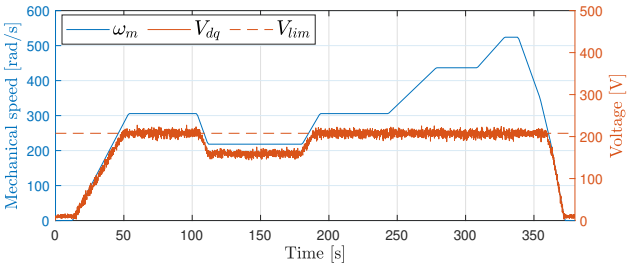

(c) Flux weakening control.

Fig. 5. OPAL-RT results for NEDC.

VI. CONCLUSIONS

A hybrid flux weakening strategy has been proposed for the calculation of current trajectories in dual three-phase IPMSMs. Polar coordinates and the normalised system representation are exploited by the algorithm to generate the current vector reference. This strategy can operate in all achievable regions (MTPA, FW, and MTPV) and correct operation is guaranteed by the feedback block even if the stator resistance is neglected or electrical parameter deviations occur. The effectiveness of the algorithm is proven by results in a driving cycle.

It is important to point out that, although this algorithm has been developed with asymmetric dual three-phase IPMSMs in mind, it can be incorporated into the control of symmetric ones or even for three-phase systems.

Currently, the dual three-phase IPMSM simulated in this work is under construction and it is expected that the proposal will be experimentally validated in the near future.

ACKNOWLEDGEMENTS

This work has been supported by the "Ministerio de Ciencia e Innovación" of the Government of Spain through the PID2020-115126RB-I00 project, by the Government of the Basque Country through project KK-2020/00077 and by the European Union's Horizon 2020 research and innovation programme under project FITGEN grant agreement No 824335.

REFERENCES

[1] T. Finken, M. Felden, and K. Hameyer, "Comparison and design of different electrical machine types regarding their applicability in hybrid electrical vehicles," in *Proc. of the International Conference on Electrical Machines*, pp. 1–5, 2008.

[2] E. Levi, "Multiphase electric machines for variable-speed applications," *IEEE Transactions on Industrial Electronics*, vol. 55, no. 5, pp. 1893–1909, 2008.

[3] K. Gopakumar, S. Sathiakumar, S. Biswas, and J. Vithayathil, "Modified current source inverter fed induction motor drive with reduced torque pulsations," *IEE Proceedings B Electric Power Applications*, vol. 131, pp. 159–164(5), July 1984.

[4] J. Karttunen, S. Kallio, P. Peltoniemi, P. Silventoinen, and O. Pyrhönen, "Dual three-phase permanent magnet synchronous machine supplied by two independent voltage source inverters," in *International Symposium on Power Electronics Power Electronics, Electrical Drives, Automation and Motion*, pp. 741–747, 2012.

[5] G. Singh, K. Nam, and S. Lim, "A simple indirect field-oriented control scheme for multiphase induction machine," *IEEE Transactions on Industrial Electronics*, vol. 52, no. 4, pp. 1177–1184, 2005.

[6] Y. Zhao and T. Lipo, "Space vector PWM control of dual three-phase induction machine using vector space decomposition," *IEEE Transactions on Industry Applications*, vol. 31, no. 5, pp. 1100–1109, 1995.

[7] J. Karttunen, S. Kallio, P. Peltoniemi, P. Silventoinen, and O. Pyrhönen, "Decoupled vector control scheme for dual three-phase permanent magnet synchronous machines," *IEEE Transactions on Industrial Electronics*, vol. 61, no. 5, pp. 2185–2196, 2014.

[8] Y. Hu, Z. Q. Zhu, and M. Odavic, "Comparison of two-individual current control and vector space decomposition control for dual three-phase PMSM," *IEEE Transactions on Industry Applications*, vol. 53, no. 5, pp. 4483–4492, 2017.

[9] M. Tursini, E. Chiricozzi, and R. Petrella, "Feedforward flux-weakening control of surface-mounted permanent-magnet synchronous motors accounting for resistive voltage drop," *IEEE Transactions on Industrial Electronics*, vol. 57, no. 1, pp. 440–448, 2010.

[10] H. Liu, Z. Q. Zhu, E. Mohamed, Y. Fu, and X. Qi, "Flux-weakening control of nonsalient pole PMSM having large winding inductance, accounting for resistive voltage drop and inverter nonlinearities," *IEEE Transactions on Power Electronics*, vol. 27, no. 2, pp. 942–952, 2012.

[11] K. D. Hoang, J. Wang, M. Cyriacks, A. Melkonyan, and K. Kriegel, "Feed-forward torque control of interior permanent magnet brushless AC drive for traction applications," in *Proc. of the International Electric Machines Drives Conference*, pp. 152–159, 2013.

[12] Y. Xu, W. Zhang, and D. Sun, "Comparative research of two flux-weakening method of PMSMs in high speed range," in *Proc. of the International Conference on Electrical Machines and Systems (ICEMS)*, pp. 1–5, 2017.

[13] Y. Li, S. Zhao, and Y. Zhao, "Stduy on flux weakening speed regulation of permanent magnet synchronous motor for vehicle," in *Proc. of the Chinese Control And Decision Conference (CCDC)*, pp. 4928–4932, 2019.

[14] T.-S. Kwon, G.-Y. Choi, M.-S. Kwak, and S.-K. Sul, "Novel flux-weakening control of an IPMSM for quasi-six-step operation," *IEEE Transactions on Industry Applications*, vol. 44, no. 6, pp. 1722–1731, 2008.

[15] S. Bolognani, S. Calligaro, and R. Petrella, "Adaptive flux-weakening controller for interior permanent magnet synchronous motor drives," *IEEE Journal of Emerging and Selected Topics in Power Electronics*, vol. 2, no. 2, pp. 236–248, 2014.

[16] N. Bedetti, S. Calligaro, and R. Petrella, "Analytical design and autotuning of adaptive flux-weakening voltage regulation loop in IPMSM drives with accurate torque regulation," in *Proc. of the IEEE Energy Conversion Congress and Exposition (ECCE)*, pp. 5884–5891, 2017.

[17] V. Manzolini, D. Da Rù, and S. Bolognani, "An effective flux weakening control of a SyRM drive including MTPV operation," *IEEE Transactions on Industry Applications*, vol. 55, no. 3, pp. 2700–2709, 2019.

[18] M. M. Ismail, W. Xu, Y. Liu, and M. Dong, "Improved torque ripple reduction method for surface-mounted permanent magnet synchronous motor in flux-weakening region," in *Proc. of the International Conference on Electrical Machines and Systems (ICEMS)*, pp. 1–6, 2019.

[19] C. Miguel-Espinar, D. Heredero-Peris, G. Gross, M. Llonch-Masachs, and D. Montesinos-Miracle, "Maximum torque per voltage flux-weakening strategy with speed limiter for PMSM drives," *IEEE Transactions on Industrial Electronics*, vol. 68, no. 10, pp. 9254–9264, 2021.

[20] Y. Hu, Z.-Q. Zhu, and K. Liu, "Current control for dual three-phase permanent magnet synchronous motors accounting for current unbalance and harmonics," *IEEE Journal of Emerging and Selected Topics in Power Electronics*, vol. 2, no. 2, pp. 272–284, 2014.

[21] S. Morimoto, M. Sanada, and Y. Takeda, "Wide-speed operation of interior permanent magnet synchronous motors with high-performance current regulator," *IEEE Transactions on Industry Applications*, vol. 30, no. 4, pp. 920–926, 1994.

[22] B.-H. Bae, N. Patel, S. Schulz, and S.-K. Sul, "New field weakening technique for high saliency interior permanent magnet motor," in *Proc. of the IAS Annual Meeting on Conference Record of the Industry Applications Conference*, vol. 2, pp. 898–905 vol.2, 2003.

[23] S.-Y. Jung, J. Hong, and K. Nam, "Current minimizing torque control of the IPMSM using ferrari's method," *IEEE Transactions on Power Electronics*, vol. 28, no. 12, pp. 5603–5617, 2013.